

Mass Estimation of Galaxy Clusters with Deep Learning II: CMB Cluster Lensing

N. GUPTA^{1,*} AND C. L. REICHARDT¹

¹*School of Physics, University of Melbourne, Parkville, VIC 3010, Australia*

ABSTRACT

We present a new application of deep learning to reconstruct the cosmic microwave background (CMB) temperature maps from the images of microwave sky, and to use these reconstructed maps to estimate the masses of galaxy clusters. We use a feed-forward deep learning network, mResUNet, for both steps of the analysis. The first deep learning model, mResUNet-I, is trained to reconstruct foreground and noise suppressed CMB maps from a set of simulated images of the microwave sky that include signals from the cosmic microwave background, astrophysical foregrounds like dusty and radio galaxies, instrumental noise as well as the cluster’s own thermal Sunyaev Zel’dovich signal. The second deep learning model, mResUNet-II, is trained to estimate cluster masses from the gravitational lensing signature in the reconstructed foreground and noise suppressed CMB maps. For SPTpol-like noise levels, the trained mResUNet-II model recovers the mass of a single galaxy cluster with a $1\text{-}\sigma$ uncertainty $\Delta M_{200c}^{\text{est}}/M_{200c}^{\text{est}} = 1.37$ and 0.51 for input cluster mass $M_{200c}^{\text{true}} = 10^{14} M_{\odot}$ and $8 \times 10^{14} M_{\odot}$, respectively. For input cluster mass $M_{200c}^{\text{true}} = 3 \times 10^{14} M_{\odot}$, these uncertainties are a factor of 1.4 larger than would be achieved by a maximum likelihood estimator (MLE) on foreground-free maps with the input noise levels, but better by a factor of 1.5 than the MLE with foregrounds.

Keywords: cosmic background radiation - large-scale structure of universe - galaxies: clusters: general

1. INTRODUCTION

The number density of galaxy clusters is a promising approach to constrain cosmological models, especially those affecting late-time structure growth (e.g. Mantz et al. 2008; Vikhlinin et al. 2009; Hasselfield et al. 2013; Planck Collaboration et al. 2016a; de Haan et al. 2016; Bocquet et al. 2019; Costanzi et al. 2019). Current and upcoming experiments are expected to collectively detect more than 10^5 galaxy clusters in the next few years, two orders of magnitude larger than current cluster catalogs. Data is already being collected by some of these experiments (e.g. *eROSITA*, SPT-3G, AdvancedACT: Predehl et al. 2010; Benson et al. 2014; Henderson et al. 2016) and others plan to start operations in a near future (e.g. LSST, Euclid, Simons Observatory, CMB-S4: LSST Science Collaboration et al. 2009; Laureijs et al. 2011; Ade et al. 2019; Abazajian et al. 2019). The dramatically larger cluster catalogs have the potential to have a huge impact on our understanding of structure growth and the expansion history of universe.

One major hurdle for extracting full cosmological information from these galaxy cluster catalogs is the calibration between the cluster mass and observables (see,

e.g. Bocquet et al. 2015; Planck Collaboration et al. 2015; DES Collaboration et al. 2020). Several techniques have been used to estimate the mass of galaxy clusters. Among these, the weak gravitational lensing of background galaxies (e.g. Johnston et al. 2007; Gruen et al. 2014; Hoekstra et al. 2015; Stern et al. 2019; McClinck et al. 2019) and the lensing of cosmic microwave background (CMB, e.g. Seljak & Zaldarriaga 2000; Dodelson 2004; Holder & Kosowsky 2004; Maturi et al. 2005; Lewis & Challinor 2006; Hu et al. 2007; Yoo & Zaldarriaga 2008; Baxter et al. 2015; Melin & Bartlett 2015; Madhavacheril et al. 2015; Planck Collaboration et al. 2016a; Geach & Peacock 2017; Baxter et al. 2018; Madhavacheril & Hill 2018; Raghunathan et al. 2019b) by galaxy clusters, have demonstrated the potential for unbiased mass measurements.

Optical weak lensing becomes difficult for high-redshift galaxy clusters due to the decreasing density of background galaxies. In contrast, CMB lensing works well for at high redshift as CMB originates at $z \sim 1100$. However, CMB lensing has its own limitations related to the raw signal-to-noise and the presence of foregrounds in CMB maps. A significant foreground for CMB lensing is the thermal Sunyaev-Zel’dovich (tSZ) effect (Sunyaev & Zel’dovich 1970, 1972) signal of cluster itself that arises due to the inverse-Compton scattering of the CMB

* nikhel.gupta@unimelb.edu.au

photons by energetic electrons in intra cluster medium (ICM). If not handled, the tSZ signal (and any other millimeter-wave signals sourced by the galaxy cluster) will bias the CMB lensing mass measurement of a galaxy cluster.

In the standard quadratic estimator (QE), the large scale CMB gradient and the small scale CMB anisotropy maps are used, and the lensing signal is extracted using the correlation between the different angular scales that are uncorrelated in the primordial CMB anisotropy map (Hu et al. 2007). Leveraging on the frequency dependence of the tSZ signal, the gradient CMB map can be freed from the tSZ that eliminates the induced correlation with the CMB anisotropy map (Madhavacheril & Hill 2018; Raghunathan et al. 2019b). While this approach eliminates the bias in gradient maps, the tSZ power in small scale CMB anisotropy map adds extra variance that can become significant for high mass clusters and low noise surveys. Few other methods are devised to reduce the lensing bias and variance due to the tSZ signal from galaxy clusters. These methods include the inpainting of gradient map based on the information from surrounding pixels (Raghunathan et al. 2019a) and tSZ template fitting (Patil et al. 2020).

The maximum likelihood estimator (MLE) on the other hand extracts optimal lensing signal from CMB temperature maps (e.g. Hu et al. 2007; Baxter et al. 2015). The approach is based on fitting the lensed CMB templates to observed CMB maps and performs better than the standard QE by a factor of two at very low noise levels in the absence of tSZ signal and astrophysical foregrounds. However, current MLEs depend on the map being clean of foregrounds and are biased when applied to maps with residual foregrounds (Raghunathan et al. 2017).

In this work, we demonstrate the first use of a deep learning network to estimate the mass of galaxy clusters from the CMB lensing signal. We employ a modified version of a feed-forward deep learning algorithm, mResUNet (Gupta & Reichardt 2020, hereafter G20) that combines residual learning (He et al. 2015) and U-Net framework (Ronneberger et al. 2015). Two separate mResUNet models are trained independently. In the first step, we reconstruct the CMB temperature maps from the simulated images of microwave sky maps. This is done by training the mResUNet-I network to learn CMB features and mitigate the foreground (tSZ and astrophysical) signals as well as instrumental noise. In the second step, we use the reconstructed CMB temperature maps and mResUNet-II network to estimate the underlying mass for individual galaxy clusters. The mResUNet-II network is trained to extract lensing fea-

tures from CMB temperature maps. After training these models for CMB reconstruction and mass estimation, we test the robustness of the process by using external hydrodynamical simulations of galaxy clusters.

The paper is structured as follows. In Section 2, we describe the simulations of microwave sky maps, the deep learning model and the parameters for its optimization. In Section 3, we present mass predictions using the images from test data sets as well as the images from the external hydrodynamical simulations of SZ clusters. In Section 4, we summarize our findings and discuss future prospects.

Throughout this paper, M_{200c} is defined as the mass of the cluster within the region where the average mass density is 200 times the critical density of universe. Unless specified, the term ‘foregrounds’ refers to both the tSZ signal and astrophysical emission. The central mass and the $1-\sigma$ uncertainty is calculated as the median and half of the difference between the 16th and 84th percentile mass, respectively.

2. METHODS

In this section, we describe the microwave sky simulations of the lensed CMB temperature anisotropy; tSZ effect; radio and dusty galaxies; and instrumental noise. We then discuss the deep learning models used to extract foreground-cleaned CMB temperature maps and to estimate the masses of galaxy clusters.

2.1. Simulations of Lensed CMB Temperature Maps

We create sets of 800 simulations at each of fifteen cluster masses, ranging from $1 - 8 \times 10^{14} M_{\odot}$ in steps of $0.5 \times 10^{14} M_{\odot}$. All clusters are assumed to lie at $z = 0.7$. These simulations include the CMB (lensed by the cluster), astrophysical foregrounds (not lensed), the effects of the instrumental beam, and instrumental noise. The simulated maps are trimmed to a box size of $10' \times 10'$ with a pixel resolution of $0.25'$. A Hanning window is applied to the outer $2'$ of the box to prepare for the convolutions in the neural network.

The first ingredient in these simulated maps is the CMB. We generate Gaussian realizations of the best-fit lensed Λ CDM cosmology for the *Planck* 2016 cosmology results Planck Collaboration et al. (2016b); the power spectrum is calculated using CAMB¹ (Lewis et al. 2000). As we do for all the fields, we generate these CMB realizations on a larger box ($60' \times 60'$) to avoid edge effects from the Fourier transforms and to be sure we capture the large-scale gradients across the final box. The CMB

¹ <https://camb.info/>

maps are then lensed by the galaxy cluster at their center. We use interpolation to handle the sub-pixel-scale deflection angles. The cluster lensing convergence profile, $\kappa(M, z)$, is based on the projected NFW profile given by (Bartelmann 1996).

To these cluster-lensed CMB maps, we add both astrophysical foregrounds unassociated with the cluster and the cluster’s own SZ signal. For the first, we create Gaussian realizations of the best-fit baseline foreground model in George et al. (2015) at 150 GHz. This model includes power from other SZ halos, the kinematic SZ effect, radio galaxies, and the cosmic infrared background (CIB). For the second, we follow G20 and add a tSZ template at the cluster position based on the GNFw profile. We scale the amplitude and size of this profile following the power law relations between the tSZ signal, mass and redshift given in Arnaud et al. (2010). We also add a 20% log-normal scatter in the peak amplitude of the tSZ profile. Neither of the foregrounds nor cluster’s own SZ signal are lensed by the cluster.

We then convolve both the cluster-lensed CMB and foreground maps by a Gaussian instrumental beam with $\text{FWHM} = 1'$. We store three combinations of these maps for each realization. The first combination map is representative of what a telescope would see; it has the sum of the CMB, foregrounds, and a realization of $5 \mu\text{K-arcmin}$ white noise. The second combination map is used as a ‘truth’ set in training the first network; it has only the CMB. The third combination map is the input for training the second network; this map has the CMB and a realization of white noise. We randomly draw the white noise level for this third map from a uniform distribution between 0 to $5 \mu\text{K-arcmin}$. Varying noise levels is designed to diversify the training set to better handle the non-Gaussian statistics in the output map from stage I (see Fig. 3). We do not use the maps from stage I for training the second stage in order to ensure that the network is not trained to recover masses using information besides lensing, for example from some residual SZ signal. The κ maps are used as the ‘truth’ sets in training the second network. All maps are then trimmed to $10' \times 10'$ and apodized as described above. We have tested training the networks after trimming the maps to larger ($20' \times 20'$) sizes at a single cluster mass; we found a small improvement for $20' \times 20'$ maps. The uncertainty decreased by a factor of 0.93 to 0.98 for $20' \times 20'$ maps, but consumed more computer resources. All results shown in this work use $10' \times 10'$ maps.

We end up with four maps per realization: the sky map with the CMB, foregrounds and $5 \mu\text{K-arcmin}$ noise; the CMB-only map; the CMB map with a noise level uniformly drawn from the range 0 to $5 \mu\text{K-arcmin}$; and

the lensing convergence κ map. Since we are interested in the cluster mass only, we replace the central pixel of each $\kappa(M, z)$ map, such that, the product of the central pixel value and the mean mass of the training sample equals M_{200c} of the cluster. The first network is trained on the sky maps to reconstruct the CMB-only maps. The second network is trained on the CMB maps with noise between 0 to $5 \mu\text{K-arcmin}$ level to reproduce the κ maps and recover the cluster mass. Figure 1 shows the examples of the sky map (\tilde{T}), reconstructed CMB-only map (\tilde{T}_{FF}) and lensing convergence $\kappa(M, z)$ map for a cluster with $M_{200c} = 4 \times 10^{14} M_{\odot}$.

2.2. The mResUNet Model

We employ mResUNet (Caldeira et al. 2019), a feed-forward Convolutional Neural Network (CNN), in the two legs of the analysis. The modified ResUNet, or mResUNet, algorithm was adapted by Caldeira et al. (2019) to do image-to-image regression, i.e. get an output image that is a continuous function of the input image, from the original ResUNet feed-forward deep learning algorithm (Kayalibay et al. 2017; Zhang et al. 2018). The mResUNet, algorithm is well suited to astrophysical problems, such as the current use case of estimating the lensed CMB signal from an image of the sky.

G20 tuned the mResUNet network by introducing dilation rates to extract small and large scale features in a CMB map, which we also use in this work. As shown in Figure 1 of G20, the framework is based on the encoder-decoder paradigm. This consists of a contracting path (encoder) to capture features, a symmetric expanding path (decoder) that enables precise localization. Each path has several convolution blocks and each of these blocks have four sub-stages. Every sub-stage has a convolution layer, an activation function and a batch normalization layer. The aim of the convolution layer is to learn features of an input map using filters that are applied to a receptive field of neighbouring pixels. Each filter is typically a $k \times k$ array with $k = 1, 3, 5, \dots$, and the size of the filter ($k \times k$) is denoted as the kernel size. For each of the four sub-stages, we apply dilations to the convolution layers with a rate of 1, 2, 3 and 4. A dilation rate of N stretches the receptive field by $k + (k - 1)(N - 1)$, thus doubling the dilation rate from 1 to 2 increases the receptive field from 3×3 to 5×5 for $k=3$. These dilated convolutions systematically aggregate multi-scale contextual information without losing resolution (Yu & Koltun 2015). The total receptive field increases for each pixel of the input image as we stack several convolution layers in the network. An activation function is applied after each convolution layer in order to detect non-linear features, leading to a highly

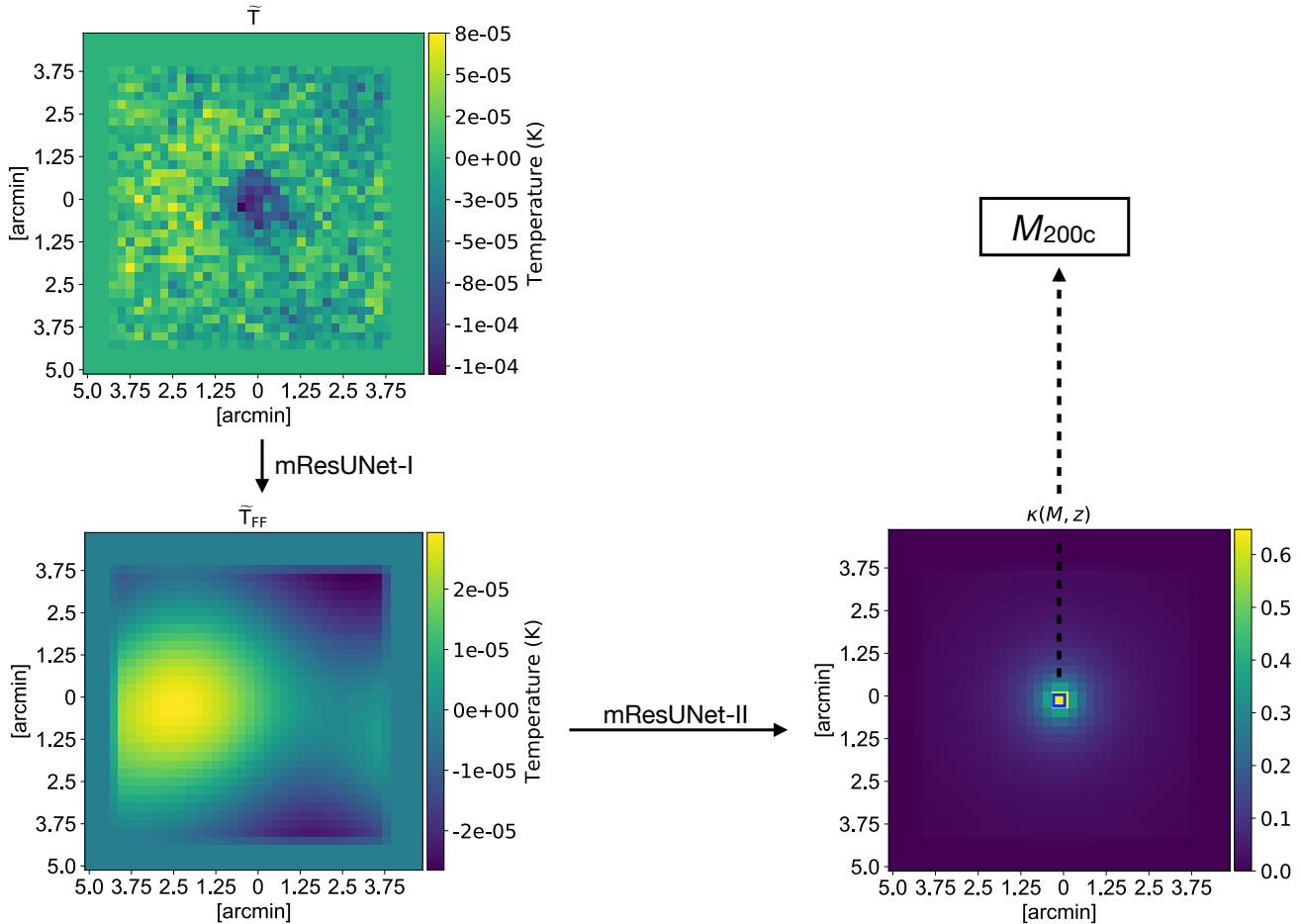


Figure 1. The work flow in the analysis: Top left panel shows an example of microwave sky CMB map (\tilde{T} , where tilde represents lensing) for a cluster with $M_{200c} = 4 \times 10^{14} M_{\odot}$ at $z = 0.7$. This map includes cluster-lensed CMB, astrophysical foregrounds, cluster tSZ signal and an instrumental white noise of $5 \mu\text{K-arcmin}$. The map is convolved with $1'$ telescope beam and apodization is applied. Several such maps for different cluster masses are used for training of the neural network (mResUNet-I) to recover foreground and noise suppressed maps (\tilde{T}_{FF}) in the first stage of the analysis. In the second stage of the analysis, the cluster-lensed CMB maps with varying white noise levels are used to train an another network (mResUNet-II) to extract the lensing $\kappa(M, z)$ maps. The trained network is then applied to the foreground-cleaned CMB maps that are output by the first network. As described in Section 2.1, the mass of cluster is then estimated from the central pixel of the extracted $\kappa(M, z)$ map.

non-linear reconstruction of input image (see Nwankpa et al. 2018, for a recent review). The batch normalization layer is helpful in improving the speed, stability and performance of the network. The input to each convolution block is always added to its output using residual connections. To avoid overfitting, we add dropout layers to the decoding phase of the network. The weights of the network are optimized using gradient descent (e.g. Ruder 2016) that involves back-propagation from the final output, back to each layer in reverse order to update the weights.

Figure 1 shows the overview of our analysis. In the first stage of analysis, we train the mResUNet-I network to reconstruct the CMB-only maps from the input

sky maps that have CMB, noise and foregrounds. In the second stage, we train the mResUNet-II network to estimate the lensing convergence map, and specifically the mass of galaxy clusters, from the recovered CMB-only maps.

2.3. Training and Optimisation

The mResUNet-I and the mResUNet-II models take images as input and output same sized images after passing through several convolutional blocks. The mResUNet-I network is trained to reconstruct \tilde{T}_{FF} maps and the mResUNet-II network is trained to extract the $\kappa(M, z)$ maps. The central pixels of the extracted $\kappa(M, z)$ maps are used to estimate the mass of clusters

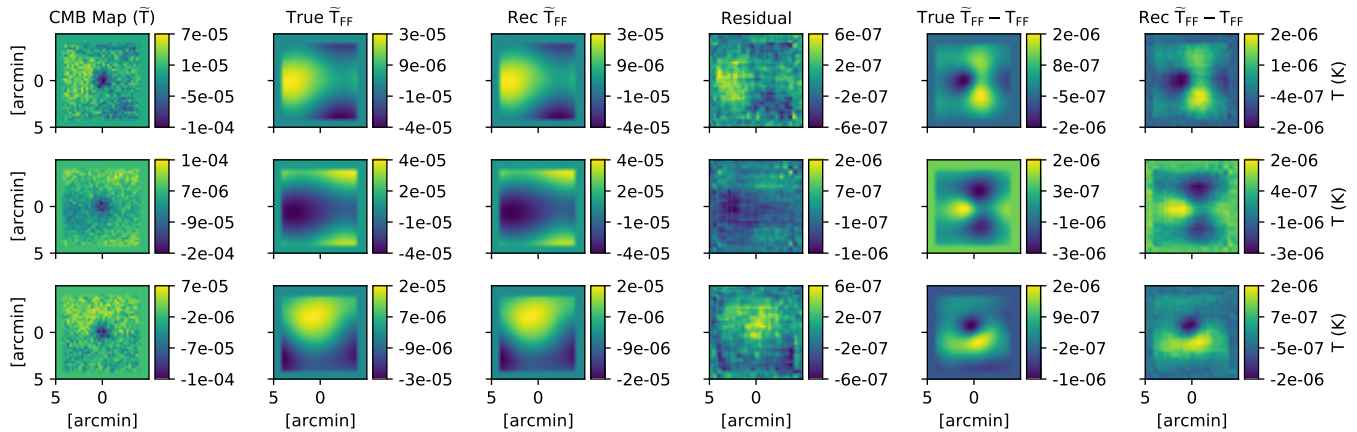


Figure 2. This figure illustrates the performance of the method for a random set of three galaxy clusters, with $M_{200c} = 4 \times 10^{14} M_{\odot}$. Each row focuses on single galaxy cluster, with the columns showing maps from different stages in the analysis. The first column shows the microwave sky (\tilde{T}), including the cluster-lensed CMB, foregrounds and instrumental noise. The second and third columns show the true and recovered CMB-only maps (\tilde{T}_{FF}). The difference between these two is shown in the fourth column, labelled ‘Residual’. The last two columns demonstrate the recovery of the desired CMB-cluster lensing signal, by showing first the true lensed - unlensed CMB map in column 5, and second the recovered lensed CMB map - true unlensed CMB map in column 6. The trained mResUNet-I model successfully reconstructs the CMB map at high accuracy including the critical CMB-cluster lensing signal.

(see Section 2.1). For training these networks, we normalize all input maps, so that the minimum and the maximum pixel value is between -1 and 1, respectively. This is done by dividing the image pixels by a constant factor across all cluster masses. The data for both networks are divided into three parts: training, validation and test sets.

The training and the validation datasets are used in the model learning process. In both legs of the analysis, the training data has 400 maps and corresponding truth sets for each cluster. We take cluster simulations with $M_{200c} = (1, 2, 3, 4, 5, 6, 7, 8) \times 10^{14} M_{\odot}$ for training and leave other for testing the model. The validation set has same properties as the training set and is used to validate the model after each epoch, where one epoch is complete when entire training data are passed through the neural network once. We use 200 maps for each cluster mass and corresponding truth sets as our validation data. The test datasets are never used in the training phase and are kept separately to analyse the trained model. We keep 200 sky maps (for each cluster mass) for testing in the first stage of analysis and use recovered CMB-only maps from these test data to estimate the mass of the individual clusters in the second stage of analysis. We use CMB maps with random realizations of white noise drawn from a uniform distribution between 0 to 5 $\mu\text{K-arcmin}$ level to train (400 maps) and validate (200 maps) the network in the second leg of analysis. In addition to the mass set used in training, we test our mResUNet-I and mResUNet-II models for cluster masses that were not the part of training and validation

process, that is clusters with $M_{200c} = (1.5, 2.5, 3.5, 4.5, 5.5, 6.5, 7.5) \times 10^{14} M_{\odot}$.

The maps in the training set are passed through the neural networks with a batch size of 4 and a training loss is computed as mean-squared-error (MSE) between the predicted and the true labels after each batch. Batch after batch, the weights of the network are updated using the gradient descent and the back-propagation. In this work, we use Adam optimizer (an algorithm for first-order gradient-based optimization, see Kingma & Ba 2014) with an initial learning rate of 0.001. After each epoch, the validation loss (or validation MSE) is calculated and we change the learning rate by implementing callbacks during the training, such that the learning rate is reduced to half if the validation loss does not improve for five consecutive epochs. In addition, to avoid overfitting, we set a dropout rate of 0.3 in the encoding phase of the mResUNet-I network which is reduced to 0.2 for the mResUNet-II network. We consider the network to be trained and stop the training process, if the validation loss does not improve for fifteen epochs.

As described in Section 2.2, each sub-stage of a convolution block in both models, has a convolution layer, an activation layer and a batch normalization layer. We set the kernel-size of each convolution layer to 3×3 and change the stride length from 1 to 2, whenever the filter size is doubled. All activation layers in these networks have a Scale Exponential Linear Unit (SELU Klambauer et al. 2017) activation functions which induce self-normalizing properties, such that, activations close to zero mean and unit variance converge towards

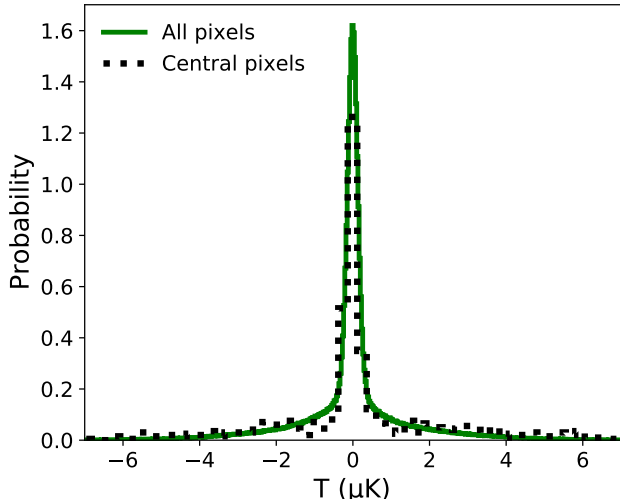


Figure 3. The distribution of the residual temperature that is the difference between the true and the recovered CMB-only maps (\tilde{T}_{FF}) as shown in the fourth column of Figure 2. The green solid and the black dotted contours show the distribution of all image pixels and central image pixels for 800 realizations of a cluster with $M_{200c} = 4 \times 10^{14} M_{\odot}$, respectively. The distribution is clearly non-Gaussian, resembling a Lorentz distribution with $\gamma = 0.5$. This indicates that the noise in the recovered \tilde{T}_{FF} maps is non-Gaussian.

zero mean and unit variance, when propagated through many network layers, even under the presence of noise and perturbations. Only for the final layer in both models, a linear (or identity) activation function is used to get same sized output images as inputs. Each network has approximately 16 million parameters and is separately trained on a single GPU using Keras with a TensorFlow backend.

3. RESULTS

In this section, we look at the performance of our trained neural network models. We show the reconstructed CMB-only maps with foreground and noise suppressed (\tilde{T}_{FF}) using the mResUNet-I network. We demonstrate that the mass of galaxy clusters can be estimated directly from the reconstructed \tilde{T}_{FF} maps using the mResUNet-II network. We find $\Delta M_{200c}^{\text{est}}/M_{200c}^{\text{est}} = 1.37$ and 0.51 for input cluster mass $M_{200c}^{\text{true}} = 10^{14} M_{\odot}$ and $8 \times 10^{14} M_{\odot}$, respectively. We test the performance of our trained deep learning models by applying them to the sky maps with more realistic tSZ signal from the external hydrodynamical simulations. Finally, we compare the S/N of the mass estimations from the current analysis to those estimated with the MLE.

3.1. Reconstruction of \tilde{T}_{FF} Maps with mResUNet-I

We use the test dataset of 200 sky maps for each of the clusters to recover the CMB-only maps using the trained mResUNet-I model. These test maps are not used for training and validation purposes and are distinct due to the Gaussian random realizations of the CMB and foregrounds as well as the 20% log-normal scatter in the estimation of the tSZ signal (see Section 2.1). The first column in Figure 2 shows the examples of the input sky maps for three random realizations of a cluster with $M_{200c} = 4 \times 10^{14} M_{\odot}$. The second and the third columns show the true and the reconstructed CMB-only maps, respectively. The fourth column shows residual signals, that is the difference between the true and the recovered CMB-only maps. The fifth column shows the difference between the true lensed and the unlensed CMB-only maps, and the last column shows the same for the recovered CMB-only maps. This demonstrates that the trained mResUNet-I model successfully reconstructs the CMB map at high accuracy including the critical CMB-cluster lensing signal.

Figure 3 shows the distributions of the residual temperature calculated as the difference between the true and the recovered CMB-only maps. The green solid and black dotted contours show the distribution of all image pixels and central pixels, respectively, for 800 realizations of the cluster with $M_{200c} = 4 \times 10^{14} M_{\odot}$. This indicates that the noise in the recovered CMB-only maps is non-Gaussian and resembles a Lorentz distribution with $\gamma = 0.5$.

3.2. Mass Estimation with mResUNet-II

We estimate the mass of galaxy clusters with the trained mResUNet-II network and using the 200 reconstructed CMB-only maps from the first stage of analysis. As the second network is trained on the cluster-lensed CMB maps with random noise realizations drawn from the uniform distribution between 0 to $5 \mu\text{K-arcmin}$ level, it extracts the κ maps using only the cluster lensing features in the reconstructed CMB-only maps. The mass of galaxy clusters is then estimated from the 200 extracted κ maps. As described in Section 2.1, this is done by multiplying the central pixel of the extracted κ maps by the mean mass of the training sample. The top panel in Figure 4 shows the estimated mass of clusters as a function of the true mass. The black data points show estimations for cluster masses that are trained in the network and the green data points describe the estimations for the interpolated mass set. All estimations are in the range of trained mass sample ($1 \times 10^{14} M_{\odot} < M_{200c} < 8 \times 10^{14} M_{\odot}$). This shows that our trained mResUNet-II model can estimate the mass of individual galaxy clusters with good precision. For instance, we

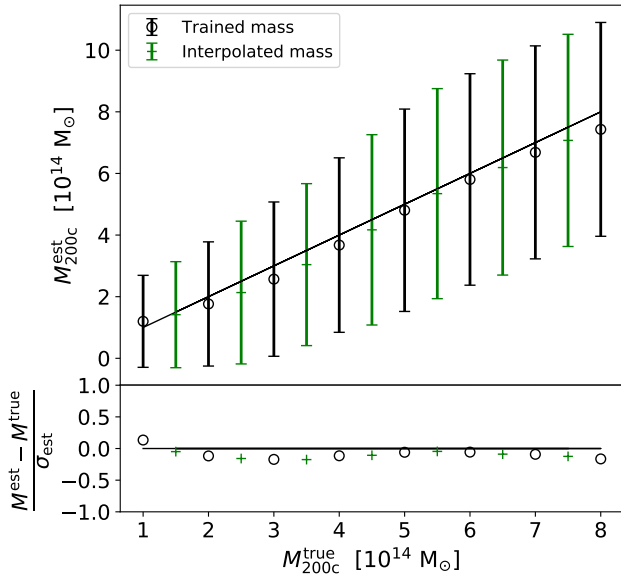


Figure 4. The trained mResUNet-II model returns unbiased mass estimates within the training range. The top panel shows the estimated and the true mass of clusters using a test data set of 200 CMB-only maps (with foreground and noise suppressed) per cluster mass that are recovered from the microwave sky maps in the stage of analysis. The black data points show results for cluster masses equal to one of the training sets. The green data points describe results for clusters with masses between the trained masses (interpolation). The bottom panel shows the significance of the difference between the estimated and true masses for each set. The bias increases for masses at the edge of the trained range, but is always much less than $1\text{-}\sigma$.

find $M_{200c}^{\text{est}} = 1.93 \pm 2.31 \times 10^{14} M_{\odot}$ for a cluster with $M_{200c}^{\text{true}} = 2.5 \times 10^{14} M_{\odot}$. The bottom panel shows the ratio of the difference between the estimated and the true mass of clusters to the estimated uncertainty. This indicates that the mass estimations with our trained neural network model are consistent with the input mass at $1\text{-}\sigma$ level.

3.3. Testing model with external hydrodynamical simulations

While we have shown machine learning works well on the symmetric Arnaud profile used for training, a reasonable question is how it will perform with more realistic (i.e. complex) cluster profiles. We explore this question by running the trained network on images drawn from clusters in the *Magneticum Pathfinder Simulation*² (MPS Dolag et al. 2016; Gupta et al. 2017; Soergel et al. 2018).

² <http://www.magneticum.org/>

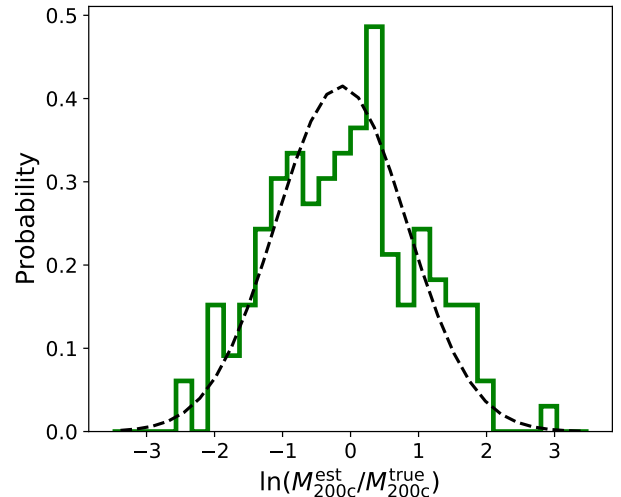


Figure 5. Test with external simulations: The deep learning models precisely recover cluster masses for the sky maps with more realistic SZ signal from the independent *Magneticum* hydrodynamical simulation. Shown is the histogram of $\ln(M_{200c}^{\text{est}}/M_{200c}^{\text{true}})$ (solid green line) for 140 clusters in the simulation. Fitting a Gaussian to this distribution yields $\sigma = 0.85$ and $\mu = -0.073$. This test verifies the universality of the trained neural networks.

The MPS is a large hydrodynamical simulation carried out as a counterpart to ongoing, multiwavelength surveys, and includes both the kSZ and tSZ effect. We take cutouts of the kSZ and tSZ maps provided with the MPS simulations at the locations of 140 galaxy clusters at $z = 0.67$ and $z = 0.73$ with $2 \times 10^{14} M_{\odot} < M_{200c} < 7 \times 10^{14} M_{\odot}$. The MPS cluster catalog lists masses in terms of the overdensity of 500 times the critical density of universe; we convert this to M_{200c} using a model of the concentration-mass relation (Diemer & Kravtsov 2015). As the MPS maps have a pixel size of $0.19'$, we interpolate these maps to match the $0.25'$ pixelation used in this work. We also convolve the SZ maps by the assumed $1'$ beam. The other signals in the mm-wave sky (the lensed CMB, instrumental noise, radio and dusty galaxies) are generated as in Section 2.1 and added to the SZ maps.

We pass the resulting maps to the two trained neural networks. Note that these networks have been trained with the symmetric Arnaud-based tSZ cluster profiles, not the MPS images. Assuming a log-normal scatter, we plot the histogram of the log difference between the estimated true masses in Figure 5. The distribution looks consistent with a log-normal scatter. We fit the distribution to a Gaussian, finding $\sigma = 0.85$ and mean $\mu = -0.073$. We conclude that despite the networks being trained on symmetric Arnaud SZ profiles, the neural networks still perform very well on realistic SZ profiles.

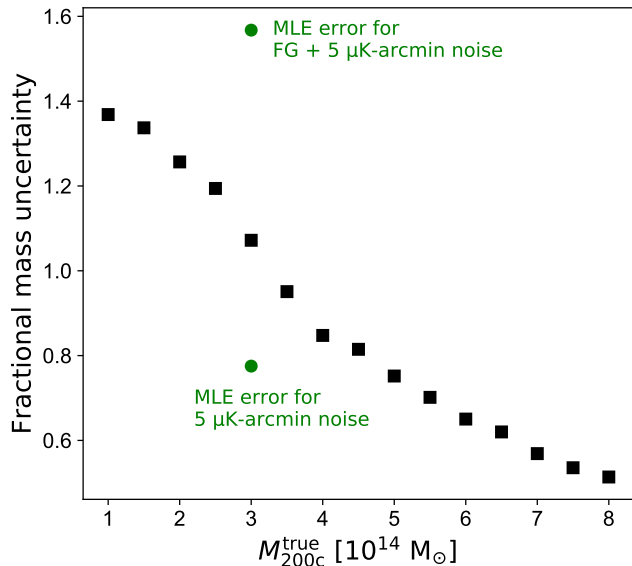


Figure 6. The fractional mass uncertainty on a single cluster as a function of input mass. The black squares show the $\Delta M_{200c}^{\text{est}}/M_{200c}^{\text{est}}$ from the current work using the recovered \tilde{T}_{FF} maps. The upper and lower green circles show the $\Delta M_{200c}^{\text{MLE}}/M_{200c}^{\text{MLE}}$ from the MLE using the noisy CMB maps with and without astrophysical foregrounds, respectively.

The two stage algorithm, using mResUNet-I and then mResUNet-II, still recovers cluster masses to good precision.

3.4. Comparison with Mass Estimations from MLE

The MLE uses pixel to pixel correlations to fit lensed CMB templates to the observed microwave sky CMB maps. The pixel to pixel covariance matrix is estimated using a set of simulated skies and is a function of cluster mass and redshift (e.g. Baxter et al. 2015). Figure 6 shows the uncertainties in our mass estimations as a function of input mass (black squares). We find $\Delta M_{200c}^{\text{est}}/M_{200c}^{\text{est}} = 1.37$ and 0.51 for input cluster mass $M_{200c}^{\text{true}} = 10^{14} M_{\odot}$ and $8 \times 10^{14} M_{\odot}$, respectively.

We compare these numbers to the uncertainties estimated from MLEs for two scenarios: (1) First, we compare the estimated mass uncertainty from MLE applied to CMB maps having a realization of white noise at $5 \mu\text{K-arcmin}$ level. The lower green circle in Figure 6 shows the $\Delta M_{200c}^{\text{MLE}}/M_{200c}^{\text{MLE}} = 0.78$ for a cluster with $M_{200c}^{\text{true}} = 3 \times 10^{14} M_{\odot}$. The uncertainty is estimated for 100,000 clusters and we scale it for one cluster as the mass estimates in present work are for individual clusters. As shown in Figure 6, the $\Delta M_{200c}^{\text{est}}/M_{200c}^{\text{est}} = 1.07$ for the same mass cluster. Thus, the mass uncertainty from MLE is a factor of 1.37 smaller than the estimates

from the deep learning model. (2) Second, we compare the estimated mass uncertainty from MLE applied to CMB maps having a realization of white noise at $5 \mu\text{K-arcmin}$ level as well as the astrophysical foregrounds (as described in section 2.1). We assume that the tSZ signal is perfectly removed from these maps. The imperfect cleaning of tSZ foreground signal can lead to significant biases in mass estimations with MLE (see section 4.6.2 in Raghunathan et al. 2017). The upper green circle in Figure 6 shows the $\Delta M_{200c}^{\text{MLE}}/M_{200c}^{\text{MLE}} = 1.56$ which is a factor of 1.46 larger than the estimates from the trained deep learning model.

The above comparisons show that the trained deep learning models put competitive constraints on the cluster masses. Note that we do not use the reconstructed CMB-only maps with suppressed foregrounds and noise to derive the MLE mass uncertainties. This is mainly due to the non-Gaussian nature of the residual noise in these maps (see Fig. 3). The application of MLE to the reconstructed CMB-only maps will require new developments and we plan to modify the MLE in our future work.

4. CONCLUSIONS

We demonstrate for the first time a two-stage deep learning algorithm that first extracts foreground-cleaned CMB maps and second estimates the mass of galaxy clusters from their gravitational lensing imprint upon the CMB map. We show that the deep learning algorithm accurately recovers galaxy cluster masses as long as the masses are within the trained mass range. For realistic skies with foregrounds, the deep learning approach recovers galaxy cluster masses with lower uncertainties than a maximum likelihood estimator (MLE).

The CMB sky maps include Gaussian realizations of CMB and astrophysical foregrounds, cluster's own tSZ signal with 20% intrinsic scatter (a foreground in this case), $5 \mu\text{K-arcmin}$ instrumental white noise and $1'$ beam smoothing. We train and validate the mResUNet-I network with 400 and 200 sky maps, respectively, for each of the eight cluster masses with $M_{200c} = (1, 2, 3, 4, 5, 6, 7, 8) \times 10^{14} M_{\odot}$. The mResUNet-II network is trained (400) and validated (200) with CMB maps having white noise randomly drawn from a uniform distribution between 0 to $5 \mu\text{K-arcmin}$ level. A test set of 200 sky maps is used to first reconstruct CMB-only maps with the trained mResUNet-I model and then to estimate the underlying cluster mass with the trained mResUNet-II model. We find that the trained models recover the input mass for individual clusters with good accuracy. For instance, we find $M_{200c}^{\text{est}} = 1.93 \pm 2.31 \times 10^{14} M_{\odot}$ for a cluster with $M_{200c}^{\text{true}} = 2.5 \times 10^{14} M_{\odot}$.

As cluster’s own SZ signal acts as a foreground for the CMB lensing signal, we test the universality of our trained models using more realistic SZ signal from the external hydrodynamical simulations. While the mResUNet-I model is trained on simplified tSZ profiles (spherically symmetric Arnaud profiles), the trained model performs well when provided CMB images with more realistic SZ profiles. We demonstrate this by taking 140 galaxy cluster cutouts from the light cones of the Magneticum hydrodynamical simulation at $z = 0.67$ and $z = 0.73$ with $2 \times 10^{14} M_{\odot} < M_{200c} < 7 \times 10^{14} M_{\odot}$. These cutouts include more complex tSZ structure from the cluster itself, kSZ signal from bulk motion of cluster, as well as the added tSZ contributions from other objects along nearby lines of sight. Our trained mResUNet-I and mResUNet-II models recover the true masses of the clusters, with no significant bias and a log-normal scatter of ~ 0.85 .

We compare the mass uncertainties from the deep learning models with those estimated from the MLE for a cluster with $M_{200c}^{\text{true}} = 3 \times 10^{14} M_{\odot}$. We find that the uncertainty from MLE $\Delta M_{200c}^{\text{MLE}}/M_{200c}^{\text{MLE}}$ is a factor of 1.4 smaller when applied on CMB maps having white noise at $5 \mu\text{K}$ -arcmin level and zero foreground power. In the presence of astrophysical foregrounds the uncertainty from MLE is a factor of 1.5 larger than the deep learning estimation.

In our future work, we plan to apply this two-stage deep learning approach to estimate galaxy cluster masses in real CMB data. Presuming no insurmountable challenges appear, deep learning would be a valuable tool for determining the masses of high-redshift galaxy clusters in ongoing and upcoming CMB surveys (e.g. SPT-3G, AdvancedACT, Simons Observatory, CMB-S4 Benson et al. 2014; Henderson et al. 2016; Ade et al. 2019; Abazajian et al. 2019). Accurate mass estimates across the full range of redshifts will be essential to fully utilizing the large, $> 10^5$ galaxy cluster samples expected from CMB, X-ray and optical surveys (e.g. *eROSITA*, LSST, Euclid Predehl et al. 2010; LSST Science Collaboration et al. 2009; Laureijs et al. 2011).

ACKNOWLEDGMENTS

We acknowledge support from the Australian Research Council’s Discovery Projects scheme (DP150103208). We thank Srinivasan Raghunathan, Sanjay Patil, Brian Nord, João Caldeira and Federico Bianchini for their helpful feedback.

REFERENCES

- Abazajian, K., Addison, G., Adshead, P., et al. 2019, arXiv e-prints, arXiv:1907.04473.
<https://arxiv.org/abs/1907.04473>
- Ade, P., Aguirre, J., Ahmed, Z., et al. 2019, JCAP, 2019, 056, doi: [10.1088/1475-7516/2019/02/056](https://doi.org/10.1088/1475-7516/2019/02/056)
- Arnaud, M., Pratt, G. W., Piffaretti, R., et al. 2010, A&A, 517, A92+, doi: [10.1051/0004-6361/200913416](https://doi.org/10.1051/0004-6361/200913416)
- Bartelmann, M. 1996, A&A, 313, 697
- Baxter, E. J., Keisler, R., Dodelson, S., et al. 2015, ApJ, 806, 247, doi: [10.1088/0004-637X/806/2/247](https://doi.org/10.1088/0004-637X/806/2/247)
- Baxter, E. J., Raghunathan, S., Crawford, T. M., et al. 2018, MNRAS, 476, 2674, doi: [10.1093/mnras/sty305](https://doi.org/10.1093/mnras/sty305)
- Benson, B. A., Ade, P. A. R., Ahmed, Z., et al. 2014, Society of Photo-Optical Instrumentation Engineers (SPIE) Conference Series, Vol. 9153, SPT-3G: a next-generation cosmic microwave background polarization experiment on the South Pole telescope, 91531P, doi: [10.1117/12.2057305](https://doi.org/10.1117/12.2057305)
- Bocquet, S., Saro, A., Mohr, J. J., et al. 2015, ApJ, 799, 214, doi: [10.1088/0004-637X/799/2/214](https://doi.org/10.1088/0004-637X/799/2/214)
- Bocquet, S., Dietrich, J. P., Schrabback, T., et al. 2019, ApJ, 878, 55, doi: [10.3847/1538-4357/ab1f10](https://doi.org/10.3847/1538-4357/ab1f10)
- Caldeira, J., Wu, W. L. K., Nord, B., et al. 2019, Astronomy and Computing, 28, 100307, doi: [10.1016/j.ascom.2019.100307](https://doi.org/10.1016/j.ascom.2019.100307)
- Costanzi, M., Rozo, E., Simet, M., et al. 2019, MNRAS, 488, 4779, doi: [10.1093/mnras/stz1949](https://doi.org/10.1093/mnras/stz1949)
- de Haan, T., Benson, B. A., Bleem, L. E., et al. 2016, The Astrophysical Journal, 832, 95.
<http://stacks.iop.org/0004-637X/832/i=1/a=95>
- DES Collaboration, Abbott, T., Aguena, M., et al. 2020, arXiv e-prints, arXiv:2002.11124.
<https://arxiv.org/abs/2002.11124>
- Diemer, B., & Kravtsov, A. V. 2015, ApJ, 799, 108, doi: [10.1088/0004-637X/799/1/108](https://doi.org/10.1088/0004-637X/799/1/108)
- Dodelson, S. 2004, PhRvD, 70, 023009, doi: [10.1103/PhysRevD.70.023009](https://doi.org/10.1103/PhysRevD.70.023009)
- Dolag, K., Komatsu, E., & Sunyaev, R. 2016, MNRAS, 463, 1797, doi: [10.1093/mnras/stw2035](https://doi.org/10.1093/mnras/stw2035)
- Geach, J. E., & Peacock, J. A. 2017, Nature Astronomy, 1, 795, doi: [10.1038/s41550-017-0259-1](https://doi.org/10.1038/s41550-017-0259-1)

- George, E. M., Reichardt, C. L., Aird, K. A., et al. 2015, *ApJ*, 799, 177, doi: [10.1088/0004-637X/799/2/177](https://doi.org/10.1088/0004-637X/799/2/177)
- Gruen, D., Seitz, S., Brimiouille, F., et al. 2014, *MNRAS*, 442, 1507, doi: [10.1093/mnras/stu949](https://doi.org/10.1093/mnras/stu949)
- Gupta, N., & Reichardt, C. L. 2020, arXiv e-prints, arXiv:2003.06135. <https://arxiv.org/abs/2003.06135>
- Gupta, N., Saro, A., Mohr, J. J., Dolag, K., & Liu, J. 2017, *MNRAS*, 469, 3069, doi: [10.1093/mnras/stx715](https://doi.org/10.1093/mnras/stx715)
- Hasselfield, M., Hilton, M., Marriage, T. A., et al. 2013, ArXiv e-prints. <https://arxiv.org/abs/1301.0816>
- He, K., Zhang, X., Ren, S., & Sun, J. 2015, arXiv e-prints, arXiv:1512.03385. <https://arxiv.org/abs/1512.03385>
- Henderson, S. W., Allison, R., Austermann, J., et al. 2016, *Journal of Low Temperature Physics*, 184, 772, doi: [10.1007/s10909-016-1575-z](https://doi.org/10.1007/s10909-016-1575-z)
- Hoekstra, H., Herbonnet, R., Muzzin, A., et al. 2015, *MNRAS*, 449, 685, doi: [10.1093/mnras/stv275](https://doi.org/10.1093/mnras/stv275)
- Holder, G., & Kosowsky, A. 2004, *ApJ*, 616, 8, doi: [10.1086/424808](https://doi.org/10.1086/424808)
- Hu, W., DeDeo, S., & Vale, C. 2007, *New Journal of Physics*, 9, 441, doi: [10.1088/1367-2630/9/12/441](https://doi.org/10.1088/1367-2630/9/12/441)
- Johnston, D. E., Sheldon, E. S., Wechsler, R. H., et al. 2007, ArXiv e-prints. <https://arxiv.org/abs/0709.1159>
- Kayalibay, B., Jensen, G., & van der Smagt, P. 2017, arXiv e-prints, arXiv:1701.03056. <https://arxiv.org/abs/1701.03056>
- Kingma, D. P., & Ba, J. 2014, arXiv e-prints, arXiv:1412.6980. <https://arxiv.org/abs/1412.6980>
- Klambauer, G., Unterthiner, T., Mayr, A., & Hochreiter, S. 2017, arXiv e-prints, arXiv:1706.02515. <https://arxiv.org/abs/1706.02515>
- Laureijs, R., Amiaux, J., Arduini, S., et al. 2011, arXiv e-prints, arXiv:1110.3193. <https://arxiv.org/abs/1110.3193>
- Lewis, A., & Challinor, A. 2006, *PhR*, 429, 1, doi: [10.1016/j.physrep.2006.03.002](https://doi.org/10.1016/j.physrep.2006.03.002)
- Lewis, A., Challinor, A., & Lasenby, A. 2000, *ApJ*, 538, 473, doi: [10.1086/309179](https://doi.org/10.1086/309179)
- LSST Science Collaboration, Abell, P. A., Allison, J., et al. 2009, arXiv e-prints, arXiv:0912.0201. <https://arxiv.org/abs/0912.0201>
- Madhavacheril, M., Sehgal, N., Allison, R., et al. 2015, *PhRvL*, 114, 151302, doi: [10.1103/PhysRevLett.114.151302](https://doi.org/10.1103/PhysRevLett.114.151302)
- Madhavacheril, M. S., & Hill, J. C. 2018, *PhRvD*, 98, 023534, doi: [10.1103/PhysRevD.98.023534](https://doi.org/10.1103/PhysRevD.98.023534)
- Mantz, A., Allen, S. W., Ebeling, H., & Rapetti, D. 2008, *MNRAS*, 387, 1179, doi: [10.1111/j.1365-2966.2008.13311.x](https://doi.org/10.1111/j.1365-2966.2008.13311.x)
- Maturi, M., Bartelmann, M., Meneghetti, M., & Moscardini, L. 2005, *A&A*, 436, 37, doi: [10.1051/0004-6361:20041785](https://doi.org/10.1051/0004-6361:20041785)
- McClintock, T., Varga, T. N., Gruen, D., et al. 2019, *MNRAS*, 482, 1352, doi: [10.1093/mnras/sty2711](https://doi.org/10.1093/mnras/sty2711)
- Melin, J.-B., & Bartlett, J. G. 2015, *A&A*, 578, A21, doi: [10.1051/0004-6361/201424720](https://doi.org/10.1051/0004-6361/201424720)
- Nwankpa, C., Ijomah, W., Gachagan, A., & Marshall, S. 2018, arXiv e-prints, arXiv:1811.03378. <https://arxiv.org/abs/1811.03378>
- Patil, S., Raghunathan, S., & Reichardt, C. L. 2020, *ApJ*, 888, 9, doi: [10.3847/1538-4357/ab55dd](https://doi.org/10.3847/1538-4357/ab55dd)
- Planck Collaboration, Ade, P. A. R., Aghanim, N., et al. 2015, ArXiv e-prints. <https://arxiv.org/abs/1502.01597>
- . 2016a, *A&A*, 594, A24, doi: [10.1051/0004-6361/201525833](https://doi.org/10.1051/0004-6361/201525833)
- . 2016b, *A&A*, 594, A13, doi: [10.1051/0004-6361/201525830](https://doi.org/10.1051/0004-6361/201525830)
- Predehl, P., Andritschke, R., Böhringer, H., et al. 2010, in *Society of Photo-Optical Instrumentation Engineers (SPIE) Conference Series*, Vol. 7732, Society of Photo-Optical Instrumentation Engineers (SPIE) Conference Series, doi: [10.1117/12.856577](https://doi.org/10.1117/12.856577)
- Raghunathan, S., Holder, G. P., Bartlett, J. G., et al. 2019a, *JCAP*, 2019, 037, doi: [10.1088/1475-7516/2019/11/037](https://doi.org/10.1088/1475-7516/2019/11/037)
- Raghunathan, S., Patil, S., Baxter, E. J., et al. 2017, *JCAP*, 2017, 030, doi: [10.1088/1475-7516/2017/08/030](https://doi.org/10.1088/1475-7516/2017/08/030)
- Raghunathan, S., Patil, S., Baxter, E., et al. 2019b, *ApJ*, 872, 170, doi: [10.3847/1538-4357/ab01ca](https://doi.org/10.3847/1538-4357/ab01ca)
- Ronneberger, O., Fischer, P., & Brox, T. 2015, arXiv e-prints, arXiv:1505.04597. <https://arxiv.org/abs/1505.04597>
- Ruder, S. 2016, arXiv e-prints, arXiv:1609.04747. <https://arxiv.org/abs/1609.04747>
- Seljak, U., & Zaldarriaga, M. 2000, *ApJ*, 538, 57, doi: [10.1086/309098](https://doi.org/10.1086/309098)
- Soergel, B., Saro, A., Giannantonio, T., Efstathiou, G., & Dolag, K. 2018, *MNRAS*, 478, 5320, doi: [10.1093/mnras/sty1324](https://doi.org/10.1093/mnras/sty1324)
- Stern, C., Dietrich, J. P., Bocquet, S., et al. 2019, *MNRAS*, 485, 69, doi: [10.1093/mnras/stz234](https://doi.org/10.1093/mnras/stz234)
- Sunyaev, R. A., & Zel'dovich, Y. B. 1970, *Comments on Astrophysics and Space Physics*, 2, 66
- . 1972, *Comments on Astrophysics and Space Physics*, 4, 173
- Vikhlinin, A., Kravtsov, A. V., Burenin, R. A., et al. 2009, *ApJ*, 692, 1060, doi: [10.1088/0004-637X/692/2/1060](https://doi.org/10.1088/0004-637X/692/2/1060)
- Yoo, J., & Zaldarriaga, M. 2008, *PhRvD*, 78, 083002, doi: [10.1103/PhysRevD.78.083002](https://doi.org/10.1103/PhysRevD.78.083002)

Yu, F., & Koltun, V. 2015, arXiv e-prints,

arXiv:1511.07122. <https://arxiv.org/abs/1511.07122>

Zhang, Z., Liu, Q., & Wang, Y. 2018, IEEE Geoscience and Remote Sensing Letters, 15, 749,

doi: [10.1109/LGRS.2018.2802944](https://doi.org/10.1109/LGRS.2018.2802944)